



## Micromagnetic understanding of evolutions of antiferromagnetic domains in NiO

Takahiro Moriyama <sup>1,2,\*</sup>, Luis Sánchez-Tejerina,<sup>3,4</sup> Kent Oda,<sup>1</sup> Takuo Ohkochi,<sup>5,6</sup> Motoi Kimata,<sup>7</sup> Yoichi Shiota <sup>1</sup>, Hiroyuki Nojiri,<sup>7</sup> Giovanni Finocchio,<sup>3</sup> and Teruo Ono<sup>1</sup>

<sup>1</sup>*Institute for Chemical Research, Kyoto University, Uji, Kyoto 611-0011, Japan*

<sup>2</sup>*PRESTO, Japan Science and Technology Agency, Kawaguchi, Saitama 322-0012, Japan*

<sup>3</sup>*Department of Mathematical and Computer Sciences, Physical Sciences and Earth Sciences, University of Messina, Viale F. Stagno d'Alcontres 31, 98166 Messina, Italy*

<sup>4</sup>*Department of Biomedical, Dental, Morphological and Functional Imaging Sciences, University of Messina, 98125 Messina, Italy*

<sup>5</sup>*Japan Synchrotron Radiation Research Institute, Sayo, Hyogo 679-5198, Japan*

<sup>6</sup>*RIKEN SPring-8 Center, Sayo, Hyogo 679-5148, Japan*

<sup>7</sup>*Institute for Materials Research, Tohoku University, Sendai, Miyagi 980-8577, Japan*



(Received 20 October 2020; revised 5 March 2023; accepted 18 April 2023; published 12 May 2023)

Antiferromagnetic domain formations and behaviors are long-standing implicit questions in magnetism and are becoming more important in recently emerging antiferromagnetic spintronics. In this paper, we experimentally investigate and numerically simulate evolutions of antiferromagnetic domains in NiO of a bulk single crystal under magnetic fields. With appropriate magnetic and crystallographic potential energy considerations, we extend a micromagnetic framework with a simulation algorithm which reproduces well the domain patterns and furnishes detailed understanding of the domain evolutions. The present work provides an important theoretical methodology to predict and understand behaviors of micromagnetic structures in antiferromagnets.

DOI: [10.1103/PhysRevMaterials.7.054401](https://doi.org/10.1103/PhysRevMaterials.7.054401)

### I. INTRODUCTION

Magnetic materials generally form magnetic domains to reduce the total energy of the system [1]. While magnetic domains in ferromagnets have been extensively studied for both fundamental and technological importance, those in antiferromagnets have not been investigated as much. However, in the recently emerging antiferromagnetic spintronics [2,3], antiferromagnetic domain formations and its dynamics are becoming implicit questions and are key to elucidating the antiferromagnetic behaviors in response to various extraneous fields such as magnetic field [4–6], spin orbit torque [7–10], and electric field [11]. Since antiferromagnets do not have spontaneous magnetization, the magnetocrystalline anisotropy and magnetoelastic energies often dominate over the negligible magnetostatic energy, which brings about the domain formations and evolutions in completely different manner than those of ferromagnets. Therefore, one often experiences a difficulty to simulate antiferromagnets with conventional micromagnetic simulation packages (e.g., OOMMF, mumax<sup>3</sup>, etc.) [12] primarily designed for ferromagnets which are not good at taking into account above-mentioned energies as well as an energy associated with the crystalline symmetry described later.

In this study, we experimentally investigate formations and evolutions of antiferromagnetic domains in NiO (001) of a bulk single crystal, which is an archetypical collinear

antiferromagnet, with a strong external magnetic field. We particularly consider and implement the crystallographic continuity into the magnetic energy calculations, we establish a unique micromagnetic simulation algorithm for the antiferromagnetic NiO, and understand the domain formations and evolutions.

### II. MODEL

NiO shows a rocksalt structure above the Néel temperature  $T_N = 523$  K and it sustains a slight rhombohedral distortion in one of the  $\langle 111 \rangle$  directions below  $T_N$  [13]. In the antiferromagnetic phase, there are two different magnetic anisotropies due to the crystalline symmetry. One is a strong magnetic *easy-plane* anisotropy lying on a  $\{111\}$  plane which is strongly coupled with the rhombohedral distortion and promotes the so-called *T* domain [Fig. 1(a)]. For instance, if the magnetic moments occupy the (111) plane, the crystal undergoes a rhombohedral contraction in the  $[111]$  direction due to a magnetic dipole interaction between the neighboring (111) planes [13]. The other is a weak threefold *in-plane* anisotropy in the  $\langle 11\bar{2} \rangle$  directions in the  $\{111\}$  plane which promotes the so-called *S* domain [Fig. 1(b)] [13]. Therefore, one *T* domain always contains a few of the three *S* domains. A combination of these magnetic anisotropies results in 12 different orientations of Néel vectors in *T* and *S* domains (Table I) [13]. Here, we label the *T* domain associated with (111) as  $T_1$  and the *S* domain with  $[\bar{2}11]$  as  $S_1$  and so on as indicated in Table I and Fig. 1. We introduce the notation  $T_n S_m$  to indicate a specific domain, where  $n$  and  $m$  are integers with  $1 \leq n \leq 4$  and  $1 \leq m \leq 3$ . For instance,  $T_1 S_1$  indicates the  $S_1$  domain

\*Present address: Department of Materials Physics, Nagoya University; mtaka@scl.kyoto-u.ac.jp

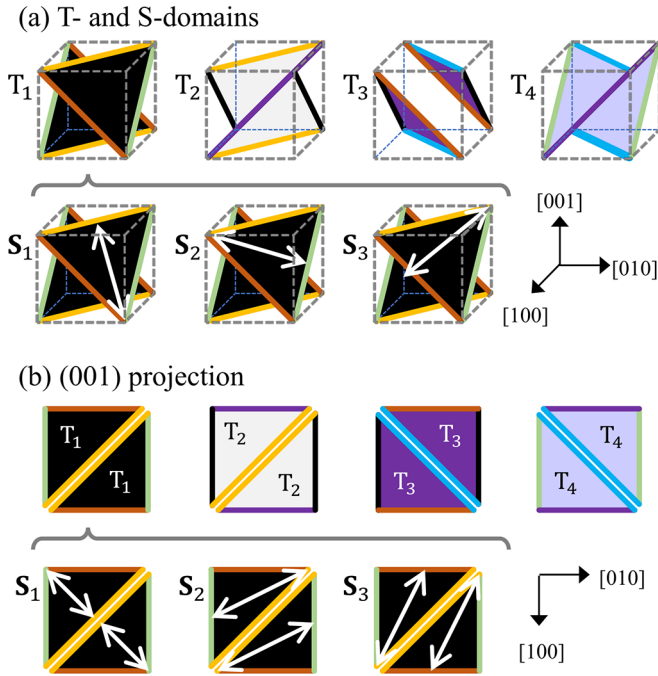


FIG. 1. Easy-plane orientations of  $T$  domains and the easy axes of the  $S$  domains. (b) (001) projection of the  $T$  and  $S$  domains. The white arrows represent the Néel vector directions. The boundary colors are consistent with the ones in Fig. 2.

belonging to the  $T_1$  domain and its Néel vector is oriented in the  $[\bar{2}11]$  direction.

Since the  $T$  domain always associates with the rhombohedral distortion, crystallographic continuity is the most important consideration to construct the micromagnetic structure [13–16]. Considering the rhombohedral symmetry, the boundaries in the same symmetry are classified by colors for each  $T$ -domain unit cell as shown in Fig. 1(a). With this classification, the connection between  $T$ -domain unit cells is preferentially made with the same color boundary (see examples in Supplemental Material (SM) Secs. I and II-a [17]).

For the micromagnetic simulations, we consider the four different potential energies involved for the stabilization of the ground state which are associated with (1) the *boundary connections* ( $U_B$ ), (2) the  *$T$ -domain connections* ( $U_T$ ), (3) the  *$S$ -domain connections* ( $U_S$ ), and (4) the *Zeeman energy* ( $U_Z$ ). While each of the potential energies is extensively explained in SM Sec. II [17], we here only describe the essences of them. The *boundary connections* consider the increase of the potential energy if a connection between different color boundaries is made (see SM Sec. II-a [17]). For the  *$T$ -domain connections*, the potential energy increases when neighboring

TABLE I. Orientations of the easy plane of the  $T$  domain and unit vectors of the easy axes of the belonging  $S$  domains.

	$T_1(111)$	$T_2(1\bar{1}\bar{1})$	$T_3(\bar{1}11)$	$T_4(\bar{1}\bar{1}1)$
$S_1$	$[\bar{2}11]/\sqrt{6}$	$[2\bar{1}\bar{1}]/\sqrt{6}$	$[211]/\sqrt{6}$	$[2\bar{1}\bar{1}]/\sqrt{6}$
$S_2$	$[\bar{1}2\bar{1}]/\sqrt{6}$	$[\bar{1}\bar{2}1]/\sqrt{6}$	$[\bar{1}21]/\sqrt{6}$	$[\bar{1}2\bar{1}]/\sqrt{6}$
$S_3$	$[11\bar{2}]/\sqrt{6}$	$[112]/\sqrt{6}$	$[1\bar{1}2]/\sqrt{6}$	$[\bar{1}12]/\sqrt{6}$

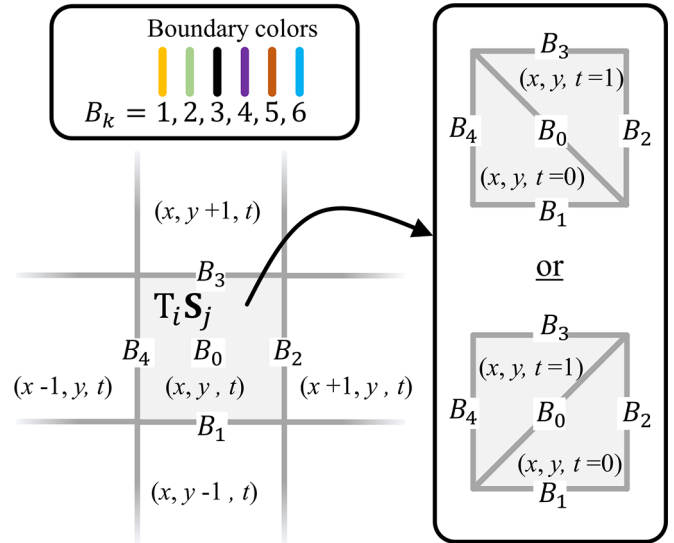


FIG. 2. Simulation unit cell at  $(x, y, t)$ , where  $t$  is the position of a half of the unit cell. Regardless of which  $T$  domain comes in, a half unit cell filled in the bottom half is labeled as  $t = 0$  and in the top half as  $t = 1$ . Definition of the six different boundaries  $B_k$  by colors.

$T$  domains are discrepant (see SM Sec. II-b [17]). Similarly, for the  *$S$ -domain connections*, the potential energy increases when neighboring  $S$  domains are discrepant (see SM Sec. II-c [17]). The *Zeeman energy* characterizes the Néel vector orientation with respect to the external magnetic field (see SM Sec. II-d [17]).

To be in line with the following experimental results, we hereinafter focus on the (001) projection of the domains [Fig. 1(b)]. With a simulation unit cell at a position  $(x, y, t)$  having the boundaries  $B_k$  (see Fig. 2), where  $t$  is a position of a half of the unit cell, we calculate the total potential energy for the total number of the simulation cells  $n$  as  $U_{\text{tot}} = \sum_x^n \sum_y^n \sum_{t=0}^1 [U_B(x, y, t) + U_T(x, y, t) + U_S(x, y, t) + U_Z(x, y, t)]$ , where  $U_B = \beta B(x, y, t)$ ,  $U_T = \tau T(x, y, t)$ ,  $U_S = \sigma S(x, y, t)$ , and  $U_Z = \gamma H S_0 Z(x, y, t)$  with the gyromagnetic ratio  $\gamma$ , the spin density of the magnetic sublattice  $S_0$ , and the applied magnetic field  $H$ .  $B(x, y, t)$ ,  $T(x, y, t)$ ,  $S(x, y, t)$ , and  $Z(x, y, t)$  are the energy function for the boundary connections, the  $T$ -domain connections, the  $S$ -domain connections, and the Zeeman energy, respectively, which are constructed by the model briefed above and discussed extensively in the SM. Depending on the strength of each connection associated with the exchange energy and the abovementioned two different anisotropy energies, the coefficients  $\beta$ ,  $\tau$ , and  $\sigma$  are set to scale each energy function. Step-by-step derivations for these energy considerations are detailed in SM Sec. II [17]. In this study, we set  $\beta = \tau = \sqrt{J_{\text{ex}} K_1}$  and  $\sigma = \sqrt{J_{\text{ex}} K_2}$ , where  $K_1$  and  $K_2$  are the *easy-plane* and the *in-plane* anisotropy energy density, respectively, and  $J_{\text{ex}}$  is the exchange energy constant. The micromagnetic simulations use the parameters  $\gamma S_0 = 5.1 \times 10^5$  [A/m],  $J_{\text{ex}} = 10^8$  [J/m<sup>3</sup>],  $K_1 = 7.2 \times 10^5$  [J/m<sup>3</sup>], and  $K_2 = 1.2 \times 10^4$  [J/m<sup>3</sup>] for the NiO which are consistent with previous reports [18,19]. A

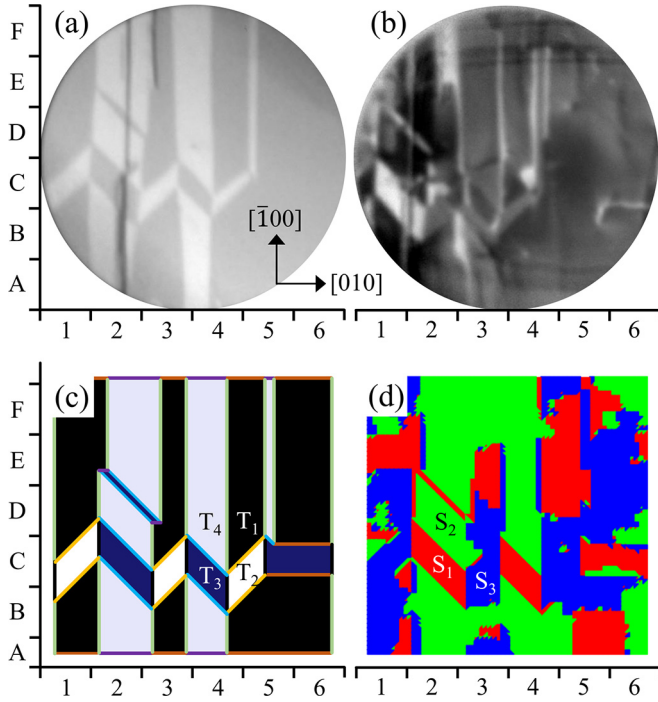


FIG. 3. XMLD-PEEM images taken with the photon energy at the O  $K$  edge (a) and Ni  $L_2$  edge (a) which respectively represent  $T$ -domain and  $S$ -domain patterns. The coordinate is shown in the inset. The reproduced  $T$ -domain (c) and  $S$ -domain pattern (d) by the micromagnetic simulation. Colors identify the boundaries of  $T$  domains.

Monte Carlo algorithm is employed to find the minimum  $U_{\text{tot}}$ . The simulation temperature is 0 K.

### III. EXPERIMENT AND DISCUSSION

Figure 3 shows the x-ray magnetic linear dichroism photoemission electron microscopy (XMLD-PEEM) images and the ones constructed by the micromagnetic simulation of a virgin (001) surface of a cleaved NiO before applying external magnetic field. The XMLD-PEEM images were taken by  $p$ -polarized x-ray beam incident with photon energies at the oxygen  $K$  edge and the Ni  $L_2$  edge which allows us to resolve mechanical distortion (or  $T$  domains) and the Néel vector orientation, respectively [20–25]. The detailed measurement conditions can be found in SM Sec. VI [17]. Figures 3(a) and 3(b) therefore *approximately* reflect the  $T$ -domain and  $S$ -domain patterns, respectively. The pattern with the oxygen  $K$  edge is found to be very sharp and shows only one contrast. On the other hand, the pattern with the Ni  $L_2$  edge is more complex with more than two contrasts. We first construct the  $T$ -domain pattern by minimizing  $\sum_x \sum_y \sum_{t=0}^1 U_B$  and reproduce the one experimentally obtained [Fig. 3(a)] (see also SM Secs. III and IV for more details). As one can see in Fig. 3(c), the reproduced  $T$ -domain pattern has no discrepancies on the boundary connections. Most importantly, it almost completely reproduces the detailed domain structures seen in Fig. 3(a). One can see that even the small details in the locations C-5, D-3, and E-2 in Fig. 3(a) are perfectly reproduced (see Fig. 6 for better comparison). Because the  $p$ -polarized x-ray beam is

incident along [010],  $T_1$  ( $T_2$ ) and  $T_3$  ( $T_4$ ) are not distinguishable by the contrast. In this image,  $T_1$  and  $T_3$  are seen darker and  $T_2$  and  $T_4$  are lighter. The contrast with the Ni  $L_2$  edge is more complex and does not directly accord with the simulated  $S$ -domain pattern [Figs. 3(b) and 3(d)]. We will discuss the XMLD-PEEM contrasts associated with the  $T$  and  $S$  domains at the end of the paper. Meanwhile, we start from these initial  $T$ - and  $S$ -domain patterns and investigate antiferromagnetic domain evolutions after applying external magnetic fields. We note that the micromagnetic consistency and stability of the Monte Carlo simulation results shown here are warranted by postprocessing them with a conventional micromagnetic solver [26].

Starting from the initial state shown in Fig. 3, we take XMLD-PEEM images after a magnetic field application and analyze them with the corresponding  $T$ -domain and  $S$ -domain patterns reproduced by the simulation. The results are displayed in Figs. 4 and 5. After a pulsed magnetic field of 24 T with a duration of 10 ms was applied in a specified direction in the sample plane (see arrows in Figs. 4 and 5), the sample was transferred to the PEEM chamber to take XMLD-PEEM images. The sample was then taken out of the chamber to apply a magnetic field in another direction. We note that the XMLD-PEEM images taken and reproduced here are therefore always in a remanent state at zero field.

The  $T$ -domain patterns observed by the O  $K$  edge are almost kept the same after the field is applied in either the [010] or [100] direction [Figs. 4(a)–4(c)]. The simulations reproduce the pattern very well [Figs. 4(f)–4(h)] which are essentially unchanged under the magnetic fields. There are some small details developed at the locations C-5, C-4, C-3, and D-2 in Figs. 4(a)–4(c) that are not reproduced by the simulations. These developments are perhaps not magnetically induced but could be due to mechanical relaxation of a rhombohedral distortion. On the other hand, the  $S$ -domain patterns reproduced by the simulation change quite a bit after the [010] or [100] fields [Figs. 5(f)–5(h)], which are consistent with the rich variations observed in the pattern taken by the Ni  $L_2$  edge [Figs. 5(a)–5(c)]. Please note that the actual Néel vector orientation depends on which  $T$  domain the  $S$  domain belongs to. Since the XMLD contrast with the Ni  $L_2$  edge is sensitive to the Néel vector orientation, the  $S$ -domain patterns do not directly reflect the XMLD contrast. We will revisit the simulated XMLD contrast at the end of this paper. These experimental observations and the simulation results can briefly be explained by the Zeeman energy term  $U_z$ . With respect to the magnetic field in the [010] direction,  $T_n S_1$  and  $T_n S_3$  ( $n = 1, 2, 3,$  and  $4$ ) can equally take the same  $U_z$  and it is smaller than  $T_n S_2$  (see Table I for the  $T_n S_m$  notation). Therefore, the system can minimize  $U_{\text{tot}}$  by switching  $S$  domains without changing  $T$  domains, leading to the invariant  $T$ -domain pattern. Similar arguments apply to the [100] field.

Remarkable changes in the domain patterns are observed when the magnetic field is applied in  $[\bar{1}10]$  and  $[\bar{1}\bar{1}0]$  directions. As seen in Fig. 4(d), the change in the  $T$ -domain pattern taken after the  $[\bar{1}10]$  field application is quite dramatic. The longitudinal domains disappear, and the diagonal domains expand along the field direction and are perfectly reproduced by the simulation [Fig. 4(i)]. Now, with the  $[\bar{1}\bar{1}0]$  field, the domains which can take the minimum  $U_z$  are limited only



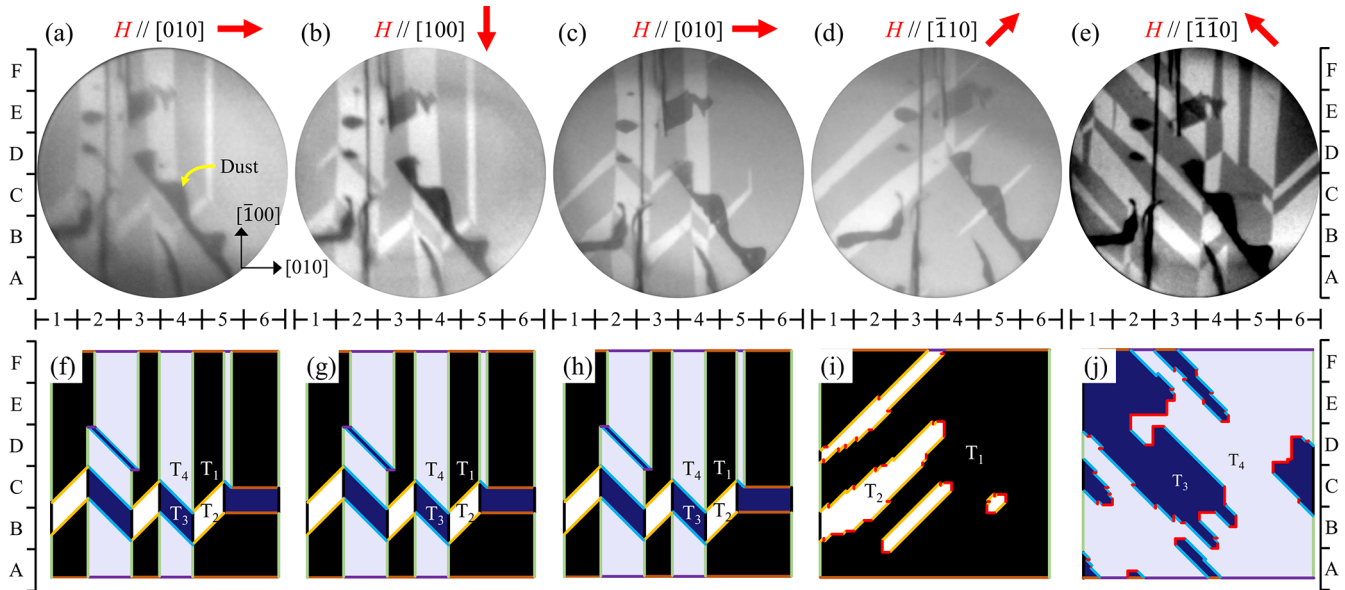


FIG. 4. (a)–(e) XMLD-PEEM images taken with the photon energy at the O  $K$  edge after each magnetic field application. Note that the black patterns scattered on the images are not related to any magnetism, but some dust adhered on the surface during the experiment (e.g., the one indicated by the yellow arrow). (f)–(j) Corresponding  $T$ -domain patterns reproduced by the simulations. The red boundaries indicate the discrepancy boundary connection, i.e., connection between different color boundaries. The alphabet-number coordinate system is referenced to specify a location.

to  $T_1S_3$  and  $T_2S_3$ . Therefore, the system switches  $T_3$  and  $T_4$  to either  $T_1$  or  $T_2$  to reduce  $U_{\text{tot}}$ . We therefore see the  $S_3$  domain everywhere [Fig. 5(i)]. Similarly, when applying the  $[\bar{1}\bar{1}0]$  field, we observed that the diagonal domains along the  $[\bar{1}\bar{1}0]$  direction become dominant as shown in Fig. 4(e). The simulation roughly reproduces similar diagonal pattern developments with  $T_3$  and  $T_4$  as shown in Fig. 4(j). With a similar argument, there is only the  $S_3$  domain in this case [Fig. 5(j)].

We now come to fully demonstrate the XMLD-PEEM contrasts with the micromagnetic simulations. The  $E$

field of the incident x-ray beam is oscillating in  $\mathbf{E} = [0, \cos \pi/3, \sin \pi/3]$  (see SM Sec. VI [17]). The  $T$ -domain contrast is given by  $|\mathbf{T}_n \cdot \mathbf{E}|$  (the larger it is, the darker the contrast) where  $\mathbf{T}_n$  is the vector normal to the easy plane in  $T_n$  [20]. It gives only one contrast because  $T_1$  ( $T_2$ ) and  $T_3$  ( $T_4$ ) are degenerated in this case (refer to Table I). Since the contrast with the Ni  $L_2$  edge is depending on the relative angle between  $\mathbf{E}$  and the Néel vector [16], it is generally given by  $|T_n \mathbf{S}_m \cdot \mathbf{E}|$ . Figure 6 shows the reproduced patterns of the XMLD-PEEM contrast with the O  $K$  edge and with the Ni  $L_2$

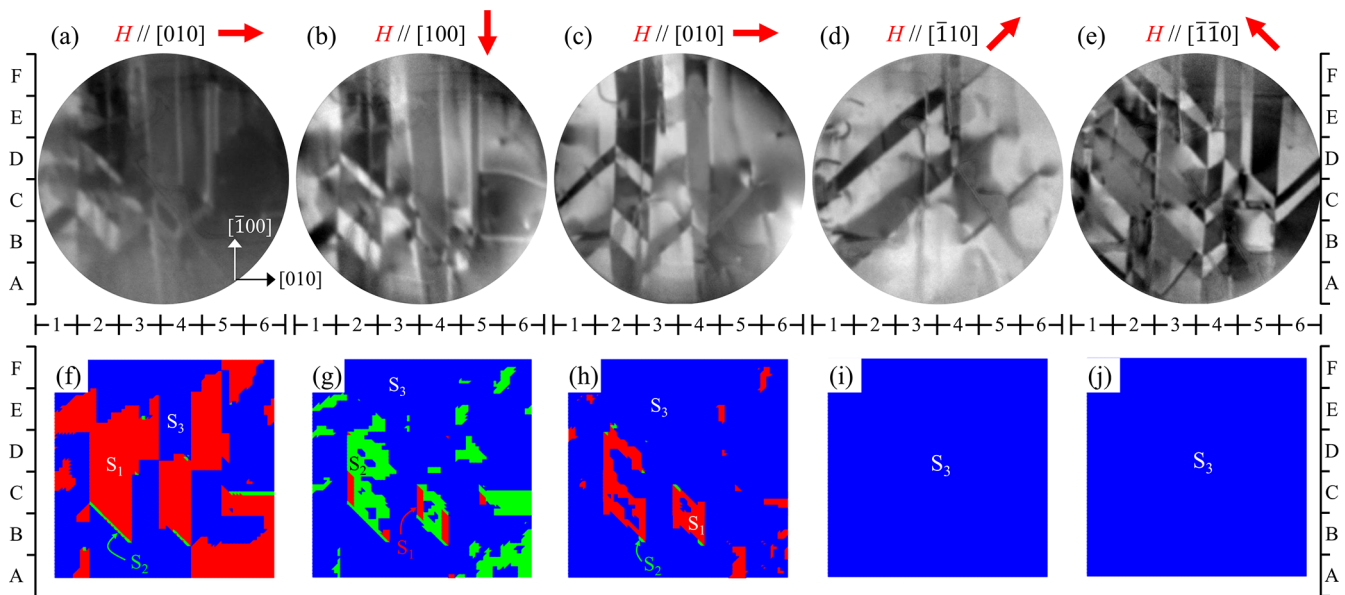


FIG. 5. (a)–(e) XMLD-PEEM images taken with the photon energy at the Ni  $L_2$  edge after each magnetic field application. (f)–(j) Corresponding  $S$ -domain patterns reproduced by the simulations.

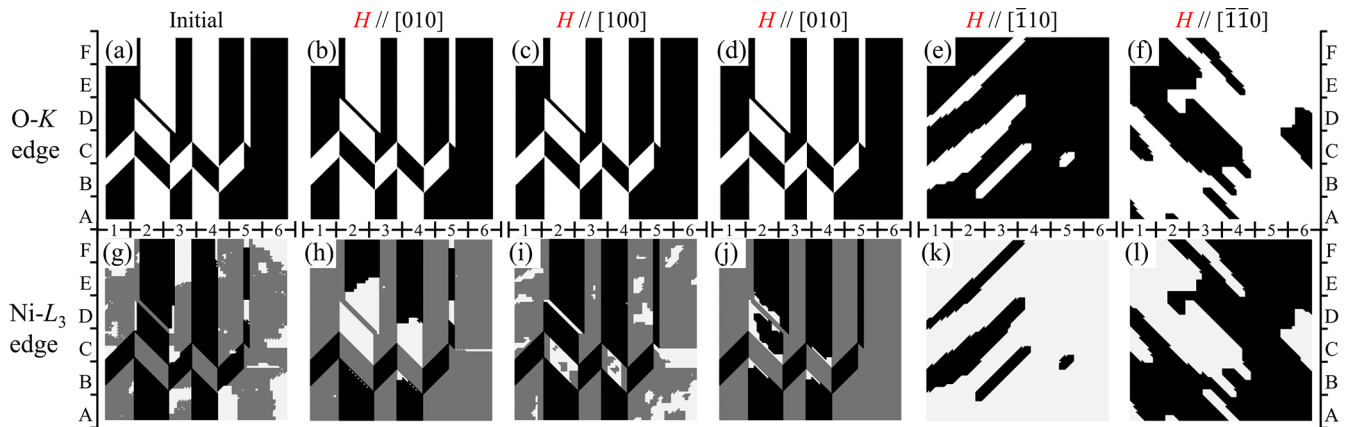


FIG. 6. Simulated XMLD-PEEM contrasts with the photon energy at the O  $K$  edge and Ni  $L_2$  edge.

edge. Those reproduced contrasts are in good agreement with the experimentally obtained ones. In particular, the patterns with the O  $K$  edge are well reproduced except for the one with the  $[\bar{1}\bar{1}0]$  field. Since the in-plane anisotropy  $K_2$ , relevant to the  $S$ -domain evolution, is relatively small, the  $S$  domain may be more easily thermally relaxed and result in some minor discrepancies between the experimental observations and the simulation results (note that the simulation assumes the temperature at 0 K while all the XMLD-PEEM measurements are performed at RT). The discrepancy might also come from a possible contribution from the anisotropic XMLD in the Ni  $L_2$  edge of NiO [27].

#### IV. SUMMARY AND CONCLUSIONS

In summary, we experimentally investigate and numerically simulate evolutions of antiferromagnetic domains in a cleaved NiO (001) under magnetic fields. First, we clearly observed, by XMLD-PEEM, the antiferromagnetic domain evolutions with a strong magnetic field and its behavior strongly depending on the magnetic field direction. Second, by considering the appropriate potential energy factors, taking into account the crystallographic symmetry as well as relevant magnetic energies, we established a unique micromagnetic simulation algorithm to reproduce details of the experimentally observed antiferromagnetic domain evolutions, which

was otherwise not possible with any conventional micromagnetic simulations. Since the micromagnetic simulation developed here is based on rather simple considerations of the potential energies, one can apply it for not only NiO but other antiferromagnets with appropriate parameters. Moreover, it is in principle possible to simulate the effects of spin orbit torque on them, which are one of the central interests for antiferromagnetic memory devices [7–9], by adding another relevant energy term. Amid growing interest in antiferromagnetic spintronics, our work provides an important methodology to predict behaviors of antiferromagnetic materials.

#### ACKNOWLEDGMENTS

XMLD-PEEM measurements were performed at BL17SU of the SPring-8 synchrotron radiation facility with the approval of the Japan Synchrotron Radiation Research Institute (JASRI) (Proposals No. 2018B0923, No. 2019A0923, and No. 2019B1417). This work was partly supported by JSPS KAKENHI (Grants No. JP19K03736, No. JP19K21972, and No. JP21H04562) and JST PRESTO Grant No. JP-MJPR20B9. T.M. would like to thank H. Moriyama for mathematical assistance. G.F. acknowledges the support under the project PRIN 2020LWPKH7 funded by the Italian Ministry of University and Research. Calculations were conducted using the supercomputer system at the Institute for Chemical Research, Kyoto University.

- 
- [1] S. Chikazumi, *Physics of Ferromagnetism* (Oxford University Press, New York, 2009).
- [2] V. Baltz, A. Manchon, M. Tsoi, T. Moriyama, T. Ono, and Y. Tserkovnyak, *Rev. Mod. Phys.* **90**, 015005 (2018).
- [3] T. Jungwirth, X. Marti, P. Wadley, and J. Wunderlich, *Nat. Nanotechnol.* **11**, 231 (2016).
- [4] A. A. Sapozhnik, M. Filianina, S. Y. Bodnar, A. Lamirand, M. A. Mawass, Y. Skourski, H. J. Elmers, H. Zabel, M. Kläui, and M. Jourdan, *Phys. Rev. B* **97**, 134429 (2018).
- [5] M. Kimata, T. Moriyama, K. Oda, and T. Ono, *Appl. Phys. Lett.* **116**, 192402 (2020).
- [6] J. Xu, C. Zhou, M. Jia, D. Shi, C. Liu, H. Chen, G. Chen, G. Zhang, Y. Liang, J. Li, W. Zhang, and Y. Wu, *Phys. Rev. B* **100**, 134413 (2019).
- [7] P. Wadley, S. Reimers, M. J. Grzybowski, C. Andrews, M. Wang, J. S. Chauhan, B. L. Gallagher, R. P. Campion, K. W. Edmonds, S. S. Dhesi, F. Maccherozzi, V. Novak, J. Wunderlich, and T. Jungwirth, *Nat. Nanotechnol.* **13**, 362 (2018).
- [8] T. Moriyama, K. Oda, T. Ohkochi, M. Kimata, and T. Ono, *Sci. Rep.* **8**, 14167 (2018).
- [9] I. Gray, T. Moriyama, N. Sivasdas, G. M. Stiehl, J. T. Heron, R. Need, B. J. Kirby, D. H. Low, K. C. Nowack, D. G. Schlom,

- D. C. Ralph, T. Ono, and G. D. Fuchs, *Phys. Rev. X* **9**, 041016 (2019).
- [10] J. Shi, V. L.-Dominguez, F. Garesci, C. Wang, H. Almasi, M. Grayson, G. Finocchio, and P. K. Amiri, *Nat. Electron.* **3**, 92 (2020).
- [11] Y. Wang, X. Zhou, C. Song, Y. Yan, S. Zhou, G. Wang, C. Chen, F. Zeng, and F. Pan, *Adv. Mater.* **27**, 3196 (2015).
- [12] See <https://math.nist.gov/oommf/> and <https://mumax.github.io/> for OOMMF and mumax3, respectively.
- [13] W. L. Roth, *J. Appl. Phys.* **31**, 2000 (1960).
- [14] T. Yamada, S. Saito, and Y. Shimomura, *J. Phys. Soc. Jpn.* **21**, 672 (1966).
- [15] K. Arai, T. Okuda, A. Tanaka, M. Kotsugi, K. Fukumoto, M. Oura, Y. Senba, H. Ohashi, T. Nakamura, T. Matsushita, T. Muro, A. Kakizaki, and T. Kinoshita, *J. Phys. Soc. Jpn.* **79**, 013703 (2010).
- [16] K. Arai, T. Okuda, A. Tanaka, M. Kotsugi, K. Fukumoto, T. Ohkochi, T. Nakamura, T. Matsushita, T. Muro, M. Oura, Y. Senba, H. Ohashi, A. Kakizaki, C. Mitsumata, and T. Kinoshita, *Phys. Rev. B* **85**, 104418 (2012).
- [17] See Supplemental Material at <http://link.aps.org/supplemental/10.1103/PhysRevMaterials.7.054401> for detailed descriptions of the experimental methods and simulation methods.
- [18] H. Kondoh, *J. Phys. Soc. Jpn* **15**, 1970 (1960).
- [19] T. Satoh, S. J. Cho, R. Iida, T. Shimura, K. Kuroda, H. Ueda, Y. Ueda, B. a. Ivanov, F. Nori, and M. Fiebig, *Phys. Rev. Lett.* **105**, 077402 (2010).
- [20] J. Stöhr, A. Scholl, T. J. Regan, S. Anders, J. Lüning, M. R. Scheinfein, H. A. Padmore, and R. L. White, *Phys. Rev. Lett.* **83**, 1862 (1999).
- [21] F. U. Hillebrecht, H. Ohldag, N. B. Weber, C. Bethke, U. Mick, M. Weiss, and J. Bahrtdt, *Phys. Rev. Lett.* **86**, 3419 (2001).
- [22] H. Ohldag, A. Scholl, F. Nolting, S. Anders, F. U. Hillebrecht, and J. Stöhr, *Phys. Rev. Lett.* **86**, 2878 (2001).
- [23] N. B. Weber, H. Ohldag, H. Gomonaj, and F. U. Hillebrecht, *Phys. Rev. Lett.* **91**, 237205 (2003).
- [24] T. Kinoshita, T. Wakita, H. Sun, T. Tohyama, A. Harasawa, H. Kiwata, F. U. Hillebrecht, K. Ono, T. Matsushima, M. Oshima, N. Ueno, and T. Okuda, *J. Phys. Soc. Jpn* **73**, 2932 (2004).
- [25] H. Ohldag, G. van der Laan, and E. Arenholz, *Phys. Rev. B* **79**, 052403 (2009).
- [26] L. Sánchez-Tejerina, V. Puliafito, P. Khalili, Amiri, M. Carpentieri, and G. Finocchio, *Phys. Rev. B* **101**, 014433 (2020).
- [27] E. Arenholz, G. van der Laan, R. V. Chopdekar, and Y. Suzuki, *Phys. Rev. Lett.* **98**, 197201 (2007).